https://doi.org/10.5194/essd-2022-57
Preprint. Discussion started: 7 June 2022

Open Access Earth System Science Data Discussions

Tropospheric water vapor: A comprehensive high resolution data collection for the transnational Upper Rhine Graben region

Benjamin Fersch[1], Andreas Wagner[2], Bettina Kamm[3], Endrit Shehaj[5], Andreas Schenk[3], Peng Yuan[4], Alain Geiger[5], Gregor Moeller[5], Bernhard Heck[4], Stefan Hinz[3], Hansjörg Kutterer[4], and Harald Kunstmann[1,2]

[1]Karlsruhe Institute of Technology, Campus Alpin (IMK-IFU), Kreuzeckbahnstraße 19, 82467 Garmisch-Partenkirchen, Germany
[2]University of Augsburg, Institute of Geography (IGUA), Alter Postweg 118, 86159 Augsburg, Germany
[3]Karlsruhe Institute of Technology, Institute of Photogrammetry and Remote Sensing (IPF), Englerstr. 7, 76131 Karlsruhe, Germany
[4]Karlsruhe Institute of Technology, Geodetic Institute (GIK), Englerstr. 7, 76131 Karlsruhe, Germany
[5]ETH Zurich, Institute of Geodesy and Photogrammetry, Robert-Gnehm-Weg 15, 8093, Zurich, Switzerland

Correspondence: Benjamin Fersch (fersch@kit.edu)

Abstract. Tropospheric water vapor is among the most important trace gases of the Earth's climate system and its temporal and spatial distribution is critical for the genesis of clouds and precipitation. Due to the pronounced dynamics of the atmosphere and the non-linear relation of air temperature and saturated vapor pressure, it is highly variable which hampers the development of high resolution and three-dimensional maps of regional extent. As a complement to the sparsely distributed radio sounding observation network, GNSS meteorology and interferometric radar satellite remote sensing can assist with their complementary high temporal or spatial resolution. In addition, data fusion with collocation and tomography methods enables the construction of detailed maps in either two or three dimensions. By assimilation of these observation based datasets into regional dynamic atmospheric models the optimal state of the tropospheric water vapor conditions can be guessed. In the following, a collection of basic and processed datasets, obtained with the above listed methods, is presented that describes the state and course of atmospheric water vapor within the range of the GNSS Upper Rhine Graben Network (GURN) region.

1 Introduction

The atmosphere of the Earth contains only up to 4% water vapor by volume or 2.5 mm global mean water equivalent. Still, atmospheric vapor is a highly effective greenhouse gas that is directly intertwined with global climate change (Stevens and Bony, 2013) and its implications for natural disasters such as floods, droughts, deluge or glacier melting. As a vital component of the hydrological cycle, water vapor represents a major driver for the generation and spatio-temporal distribution of clouds and precipitation. Vertically integrated water vapor exhibits high variability of up to 0.5 mm within a few kilometers range and sub-hourly intervals (Vogelmann et al., 2015; Steinke et al., 2015). The continuous, extensive quantification of water vapor remains a challenge: while regional atmospheric models enable the simulation of the distribution of hydrometeorological

https://doi.org/10.5194/essd-2022-57
Preprint. Discussion started: 7 June 2022

variables in space and time at high resolution (Steinke et al., 2019; Giorgi, 2019), their skill is often limited by insufficient initial conditions or inadequate parameterizations of subgrid processes (Prein et al., 2015).

Water vapor is principally regarded as a source of noise in geodesy and remote sensing applications. The humidity of the Earth's atmosphere induces delays and distortions of high temporal and spatial fluctuations in microwave signals, which cannot be eliminated by multi-frequency measurements and have to be quantified during the data processing. Thus observations of Global Navigation Satellite Systems (GNSS) and Interferometric Synthetic Aperture Radar (InSAR) provide valuable contributions (GNSS: high temporal resolution; InSAR: high spatial resolution) for reconstructing the integrated water vapor (IWV) along the path from the satellites to the observation site on the Earth's surface (Bevis et al., 1992; Hanssen, 2001). Interpolation and approximation techniques like, e.g., least-squares collocation or kriging enable a sophisticated fusion of GNSS and InSAR products. In addition, the tomography-based evaluation of these data even allows generating three-dimensional fields of the water vapor distribution in space and time.

In this study, we present the interdisciplinary, high resolution dataset of Fersch et al. (2021) of tropospheric water vapor and associated variables that incorporates all of the above mentioned methods, i.e. GNSS, InSAR, and regional atmospheric modeling, to provide a best guess of tropospheric water vapor for the transborder Upper Rhine Graben region of Germany, Switzerland, and France where an extensive GNSS observation network is located. In the following, we review concisely the different methods of tropospheric water vapor assessment before we describe the data collection and its generation in detail. Finally we evaluate the dataset with independent observations. The abbreviations and acronyms used in the text are summarized in Tab. B.

2 Methods for tropospheric water vapor assessment

As tropospheric water vapor concentrations are highly changeable with space and time, the techniques for their assessment need to be likewise precise. The common observational methods are usually good in certain aspects but come also with crucial drawbacks. Radio sounding with balloon sondes, for example, provides measurements of pressure, temperature, wind, and humidity at high vertical resolution. However, due to the effort of assembling the device and because of the sparse density of release stations, the spatial distribution of such measurements allows only for local or large scale applications, such as airfield control or numerical weather prediction. Other methods like, e.g., satellite remote sensing, allow for higher spatial resolution, but at the cost of vertical integration or reduced temporal resolution.

Obviously, the combination of different observation methods depicts a way to overcome the limitations of the individual techniques. Similarly, dynamical atmospheric models can provide a best guess of the tropospheric water constituents if observations are ingested by data assimilation.

In the following, we provide a brief overview of the common methods for tropospheric water vapor observation and modeling approaches and highlight how different data sources can be combined for the sake of added value.

https://doi.org/10.5194/essd-2022-57
Preprint. Discussion started: 7 June 2022

2.1 Observation

2.1.1 Point profiles

Local profiles of tropospheric water vapor conditions can be obtained with radio sondes, ground-based radiometry, or laser techniques. Radio sounding, typically performed with weather balloons, provides in situ measurements for temperature, pressure, and humidity for many stations globally (Brönnimann, 2015). According to Rocken et al. (2004), the global radiosonde network has about 850 stations with at least two releases per day (00 and 12 UTC). With inter-station displacements of several hundreds of kilometers even for central Europe, the measurements do not qualify for assessments of local high resolution tropospheric water vapor fields but are nevertheless valuable for the validation of other observation techniques (e.g., Divakarla et al., 2006; Reale et al., 2008; Jin et al., 2011) or in combination with satellite observations on the global scale (e.g., Randel et al., 1996; Shi et al., 2016). Ground-based microwave radiometers and infrared spectrometers provide tropospheric profiles of temperature and humidity for direct and slanted paths but require the application of complex retrieval algorithms. According to Löhnert et al. (2009), accuracies for humidity can be as good as 0.25 – 0.5 g m^{-3} during clear sky conditions but the method is limited if clouds are present. For complex terrain, Massaro et al. (2015) found that within the boundary layer, detailed humidity profiles cannot be derived with the frequencies used. Nevertheless, with accuracies below 1 kg m^{-2} the method is well suited for vertical integrals of water vapor (Almansa et al., 2020) but the measurements are mostly restricted to the lower troposphere (Feltz et al., 2003; Pospichal and Crewell, 2007; Fersch et al., 2020).The light detection and ranging (lidar) method (e.g., Klanner et al., 2021) is a further way to obtain high resolution water vapor profiles with high accuracies. The complexity of ground based radiometers and lidar systems has so far prevented the realization of such kind of networks meaning that no observations of tropospheric water vapor profiles are available at the kilometer to sub-kilometer resolution.

2.1.2 GNSS derived tropospheric variables

The ground-based GNSS technique for the monitoring of atmospheric water vapor was implemented in the early 1990s (Bevis et al., 1992). The GNSS satellite signals received at the Earth's surface are delayed by the atmosphere due to refraction. The propagation delays of the GNSS signals from slant paths can be converted to vertical with mapping functions, and thus zenith total delay (ZTD) is obtained. The ZTD can be decomposed into two parts, the zenith hydrostatic (or dry) delay (ZHD) and zenith wet delay (ZWD). The ZHD can be precisely modeled with the measured surface pressure P_s (Saastamoinen, 1972; Davis et al., 1985). The ZWD is then calculated as the difference between ZTD and ZHD, and because of its relation with atmospheric water vapor, it can be converted to IWV utilizing the atmospheric weighted mean temperature T_m (Bevis et al., 1994).

With tens of thousands of GNSS stations worldwide, the ground-based GNSS technique provides valuable information about the water vapor variability. With key advantages of all-weather operability, high accuracy, high temporal resolution, and wide distribution over lands (Jones et al., 2019), GNSS tropospheric estimates became an important data source for meteorological and climatological applications. For example, it is being used to observe the water vapor variability during extreme weather events (e.g., Zhu et al., 2020). In addition, long-term time series of IWV derived by ground-based GNSS contain valuable information about the water vapor feedback effect due to climate change (e.g., Alshawaf et al., 2018; Yuan et al., 2021).

The accuracy of the IWV retrievals is limited by the uncertainty of the ZTD estimates as well as the availability and quality of P_s and T_m observations at the GNSS stations. Ideally, P_s and T_m can be accurately measured by synoptic barometers and co-located radiosondes, respectively. In this case, the uncertainty of GNSS-derived IWV can reach 0.6 $\mathrm{kg\,m^{-2}}$ (Ning et al., 2016). However, not every GNSS station is equipped with a barometer and only few stations are co-located with radiosondes. Hence, accurate P_s and T_m obtained from atmospheric reanalyses or numerical weather predictions (NWP) have been used in the retrieval of GNSS IWV (e.g., Wang et al., 2005). In this work, we estimate the IWV from GNSS signals by incorporating the latest ERA5 reanalysis and calculated the ZTD with sophisticated data processing strategies and models (see Sec. 3.2).

2.1.3 InSAR derived tropospheric variables

Similar to the propagation delay measured with GNSS, the radar signal of the Synthetic Aperture Radar (SAR) satellites experiences a phase delay due to water vapor in the atmosphere (Hanssen, 2001, chap. 3.4). Interferometric analysis of two or more SAR acquisitions of the same area reveals the difference of integrated phase delay between these acquisition times along the SAR line of sight (LOS), i.e., along the travel path between the sensor and the observation point on the ground (Heublein, 2019).

The high spatial resolution of the InSAR data compared to other meteorological spaceborne instruments makes them attractive to address meteorological questions (Hanssen, 2001, chap. 6). Space-borne C-band SAR instruments as, e.g., on the European Remote Sensing satellites (ERS-1/2) and the Envisat satellite are successfully used to construct water vapor maps (e.g., Hanssen, 2001; Alshawaf et al., 2015b; Heublein et al., 2019). The higher sensitivity and resolution of X-band sensors offer an even more detailed analysis as shown, e.g., by Qin et al. (2013) for an urban setting. In turn, the wide footprint of the C-band sensors on the current Sentinel-1 (A/B) satellite missions enable large areas to be investigated, still with a moderately high resolution (e.g. Mateus et al., 2017).

SAR satellites are usually deployed at sun-synchronous low earth orbits. SAR-instruments are side looking, imaging in slant direction with usual incidence angles between 18°-50°. The integrated delays are therefore observed along a slant ray, corresponding to the LOS. While the incidence angle is variable across the scene, it is constant over time for a specific point on the ground, since the same orbits must be selected to achieve a coherent interferometric signal. In a first approximation the slant delays can be mapped with, e.g., the cosine function to zenith delays.

A main issue of using InSAR data over long periods is the decorrelation of the signal, as soon as the reflection characteristics of the scatterers on ground begin to change over time. Therefore, only long-term stable points, so called Persistent Scatterers (PS) are used (Hooper et al., 2007; Ferretti et al., 2001). Naturally, coherent PS points are irregularly distributed with high PS density in urban areas and sparse PS occurrence in rural and vegetated areas. PS interferometry (PSI) is widely used for small and large scale geodetic monitoring as well as tectonic deformation studies (Crosetto et al., 2016).

For using PSI in meteorological applications, it is important to keep in mind that InSAR-based measurements are measurements of phase differences. They are relative with respect to an arbitrary reference in space and time and therefore also referred to as double differential measurements. Spatial differences are resolved by phase unwrapping, up to an unknown absolute value, i.e. the unknown datum of the reference point at reference time. For retrieving absolute values of IWV, it is necessary to resolve also the temporal differences by adding the unknown absolute value. To circumvent this, common PSI techniques rely on multiple interferograms of the same area, a so-called interferogram stack, usually consisting of more than 30 interferograms. With such a large number of acquisitions, the individual differential measurements are assumed to follow a stochastic process with an average value of zero at each PS point. This led to the common approach of including the "zero-mean assumption" which bypasses the assignment of a specific true datum to a reference point, by considering the stochastic mean to be zero for each point independently (Gernhardt, 2011). The resulting single differential delays are also called Atmospheric Phase Screens (APS) (Parker et al., 2015), which show the acquisition specific variation from the mean value, but are still missing above mentioned datum in contrast to total delay products. However, the zero-mean approach does not reflect the true conditions at all. In reality, the stochastic mean of differences may show variations from zero in spatial domain and may also be dependent on the number of acquisitions and the covered time period.

Whereas the benefit of InSAR-derived zenith delays is the high spatial resolution and thus information on small scale variation of ZTD in the atmosphere, large scale regional trends and the absolute datum are less reliable and prone to errors due to the differential nature of the interferometric measurement, but also due to additional signal components like crustal tides and tidal loading. Also residual orbital errors cause long wavelength signals, so called phase ramps, which cannot be separated from large scale spatial trends in IWV or deformation (Bähr and Hanssen, 2012). Thus, further knowledge or external data needs to be introduced as additional constraint to solve the datum defect and adjust spatial trends, i.e. the signal component with long wavelengths of the estimated IWV in order to obtain the final product of absolute IWV. Alshawaf et al. (2015a) use a two-step approach to derive reliable absolute IWV maps from Envisat SAR data. First, a least-squares inversion is applied to PSI delays under the constraint of zero temporal mean, whereby the PSI delays have been low-pass filtered before to suppress long-wave signal. Subsequently, these maps are combined with complementary maps from GNSS which provide more reliable absolute and long-wave IWV but at low spatial resolution. Comparing the final combined IWV maps with IWV maps from the MEdium Resolution Imaging Spectrometer (MERIS) onboard the Envisat satellite, shows good spatial correlation of up to 92%. The study of Pichelli et al. (2014) in turn uses MERIS data to constrain the long-wave IWV and the absolute datum.

2.2 Numerical atmospheric modeling and data assimilation

The performance of numerical weather prediction (NWP) and climate models typically goes in line with the accuracy of the simulated tropospheric and in particular the planetary boundary layer (PBL) water vapor fields (Gallus and Segal, 2001; Jochum et al., 2004; Kunz et al., 2014; Jiang et al., 2020). All of the global circulation models that are employed for operational forecasting or retrospective analyses (reanalyes), ingest vast amounts of atmospheric water vapor observations, mostly based on satellite remote sensing. The benefits of this practice are well proven, e.g, for the Integrated Forecasting System (IFS) of the European Centre for Medium-Range Weather Forecasts (ECMWF, Andersson et al., 2007) or the ERA-Interim reanalysis of ECMWF (Dee et al., 2011). While the global operational NWPs develop towards convection resolving resolutions (~13 km for the Global Forecasting System GFS, (Zhou et al., 2019) and ~9 km for ECMWF's IFS), the global reanalyses stay a bit behind with resolutions of up to ~30 km for ECMWF's ERA5. A further increase in spatial resolution can be achieved with limited area models (LAM) that perform a downscaling for subregions of the global models. Typically, LAMs exhibit more detailed process descriptions as, for example, with a non-hydrostatic formulation of vertical motion, the consideration of air compressibility, or accoustic-gravity waves. The quantiative performance of LAMs depends on the quality of initial state and on time-varying boundary conditions.

The incorporation of additional water vapor information even on a smaller scale is possible through data assimilation. The positive impact of the assimilation of InSAR data (Pichelli et al., 2014; Mateus et al., 2016) and GNSS stations (Pondeca and Zou, 2001; Poli et al., 2008; Boniface et al., 2009; González et al., 2013; Lindskog et al., 2017; Giannaros et al., 2020) is shown for numerous studies and regions. InSAR provides very high spatial resolution information, but only about every 4 days. GNSS data, on the other hand, have a high temporal resolution, for example hourly, but depict point values.

In this study, we apply the 3-dimensional variational assimilation system (3D-Var) provided by WRF (Barker et al., 2003, 2004) to assimilate both kind of data as well as additional synoptic station data. Data assimilation merges atmospheric models and observations, while considering their respective error statistics, to achieve an improved initial state. Variational data assimilation schemes accomplish this step by iteratively minimizing a cost function. For further information we refer to Ide et al. (1999), Barker et al. (2003), and Barker et al. (2004).

2.3 Data fusion

Each of the above discussed techniques for atmospheric water vapor estimation has specific strengths and weaknesses. The fusion of different data products and modeling approaches allows to exploit the complementing characteristics, so that the IWV estimation gets more accurate, reliable and robust.

2.3.1 Fusion of GNSS and InSAR

Although the atmosphere affects GNSS and InSAR similarly, their tropospheric products have differing characteristics, mostly because of their different geometric setting and due to the fact that GNSS relies on sparse, though high-precise 3D point determination on ground, while PSI relies on opportunistic, appearance based but less accurate point scatterer detection. On the one hand, the most typical GNSS tropospheric product is the ZTD, an absolute measurement (at meter level), which represents the integral of the refractivity in the zenith direction, provided at cm level accuracy nowadays (Teunissen and Montenbruck, 2017). The ZTDs are provided with a high temporal resolution such as hourly or even every 5 minutes. However, the spatial resolution is relatively low depending on the density of GNSS networks. On the other hand, InSAR retrieved atmospheric maps consist of relative tropospheric delays (at cm level) obtained at very low temporal resolution (days, weeks or even months), but with a very high spatial density up to meter level. The characteristics of GNSS and InSAR in space and time are depicted in Figure 1. In this paper, we aim to exploit the synergies of both techniques by combining their tropospheric delays, to retrieve enhanced water vapor related products (delays or refractivities). For this purpose, we fuse GNSS ZTDs with InSAR differential slant total delays (ddSTD) in the least squares collocation software COMEDIE (Collocation of Meteorological Data for Interpretation and Estimation of Tropospheric Path Delays, Eckert et al., 1992a, b), upgraded to process the measurements

https://doi.org/10.5194/essd-2022-57
Preprint. Discussion started: 7 June 2022

from the different techniques simultaneously. Shehaj et al. (2020) describes the framework to combine GNSS and InSAR tropospheric delays, with the goal to retrieve tropospheric delays at any point of an investigated area. The same principles of combination is applied to the dataset discussed in this paper.

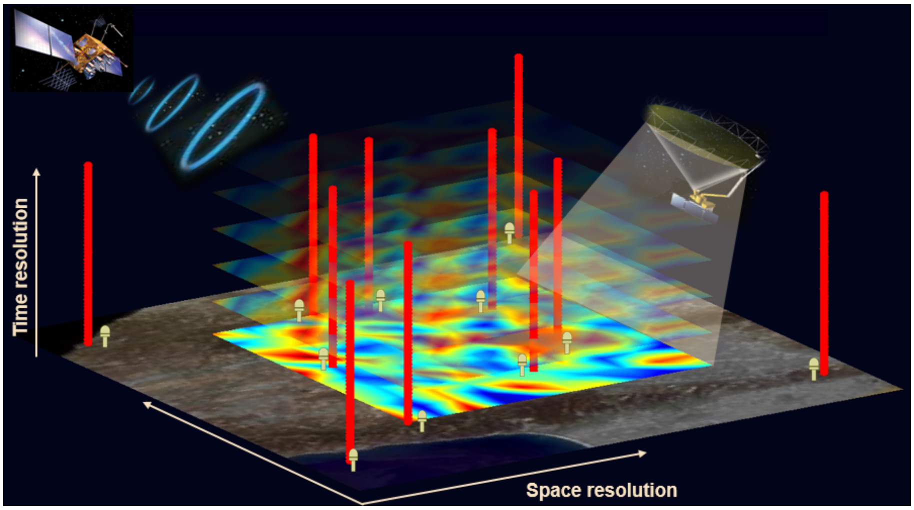

Figure 1. Co-located GNSS and InSAR techniques have complementary characteristics in space and time. (from Shehaj et al., 2020).

2.3.2 Tomography

GNSS tomography allows to resolve the distribution of the water vapor content in 4D (space and time), thus the height profiles of the water vapor can be determined (Moeller, 2017). The basis of most tomography software packages are slant path delays. In tomography, the atmosphere in the investigated area around the GNSS network is discretized in a 3D voxel model. By exploiting the relation between the slant delays and the geometric ray paths, refractivity N in each of the atmospheric voxels is obtained.

In this work, an alternative tomography approach is suggested, based on the collocation of ZTDs and STDs using software COMEDIE. The functional and stochastic models to retrieve the refractivity are obtained by forming the derivatives of the ZTD model with respect to height, as detailed in Sec. 3.5 and Hurter (2014). When combining InSAR measurements with GNSS measurements to obtain refractivity fields, the stochastic models that connect the InSAR slant delays with the refractivity, are simply the models relating the zenith delays with refractivity mapped in the slant direction; this is clear since we treat the slant delays as mapped zenith delays in the slant direction (Shehaj et al., 2020).

3 Dataset description

The dataset presented in this work was produced with the aim to provide the best possible assessment of regional, high resolution tropospheric water vapor fields, founded on established observation methods and data assimilation. For this purpose, we selected the area of the GNSS Upper Rhine Graben Network (GURN, Fig. 2) where GNSS, InSAR and radiosonde obser-

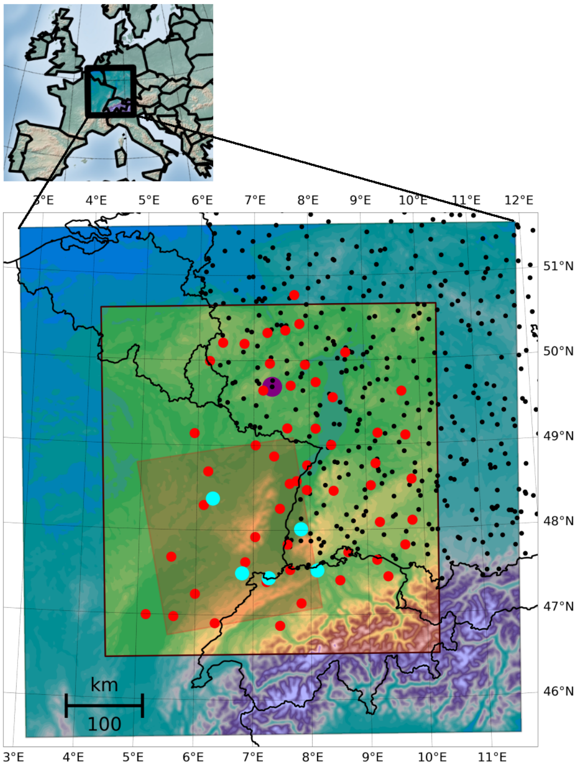

Figure 2. WRF domain (650 x 670 km) and evaluation area (440 x 460 km) with 56 GNSS stations for assimilation and tomography (red), 5 GNSS stations for validation (cyan), 245 synop stations (black) and the radiosonde station Idar-Oberstein (purple). The red area marks the core region where all datasets are available.

vations are available. We derived data products from different combinations and fusions of the individual observations and by assimilation with the limited area Weather Research and Forecasting modeling system (WRF-ARW Skamarock and Klemp, 2008). As illustrated in Fig. 3, the collection features IWV, ZTD, ZWD, WVD, and ddSTDP, derived from GNSS, SAR, and atmospheric modeling techniques. To cover the four characteristic seasons of the northern hemisphere, we selected four investigation periods for which we processed all of the data products (11 – 22 Apr 2016, 13 – 24 Jul 2018, 16 – 31 Oct 2018, 06 – 21 Jan 2017). Some of the individual datasets, i.e., the processed InSAR scenes and the GNSS ZTDs extend beyond those preselected periods or the boundaries of the GURN study region. Our intention was to provide the data as comprehensive as possible to foster further scientific studies. For better comparability, the same variables were determined for all datasets: Integrated Water Vapor (IWV) for 2D data and water vapor density for 3D data. In addition, the ERA5 reanalysis is used for all conversions that require additional meteorological input such as pressure and temperature. Moreover, we document the full processing chain so that it can be reproduced by others or repeatedly be applied as more recent data or alternative products

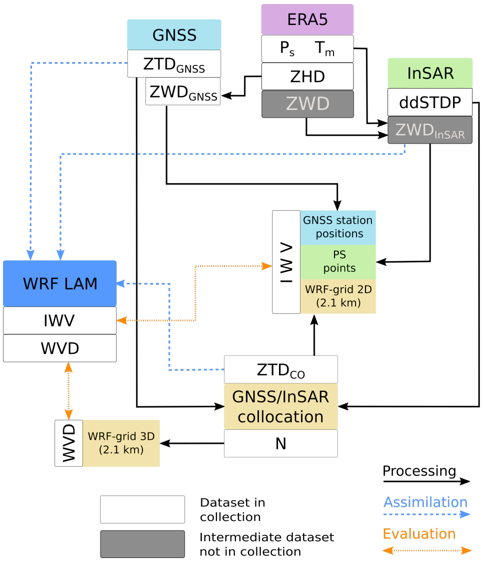

Figure 3. Dataset overview sketch. The lines depict the following pathways: black – data processing, blue – data assimilation, orange – evaluation.

become available. In the following, we describe the characteristics of the study region and the methods that have been used to provide the individual and the combined data products.

3.1 Study region

The core region is defined by the transnational GURN that was originally established for the investigation of tectonic activities (Mayer et al., 2012). It encompasses the southwestern part of Germany and the eastern part of France with the Upper Rhine Graben (URG) in the center, the Black Forest in the east, and the Vosges in the west plus a small area of north-western Switzerland (Fig. 2).

The Upper Rhine Valley is one of the warmest regions of Germany with lower annual rain amounts (approx. 600 mm a^{-1}), but with a high convective activity in the summer months. Up to 1500 mm a^{-1} of annual rain amounts are measured in the low mountain ranges of the Black Forest, the Vosges and the Swiss Jura and about 1000 mm a^{-1} in the flatter western and northwestern area.

3.2 GNSS derived IWV and ZTD

The global positioning system (GPS) observations of 66 stations of the GURN were used to estimate IWV. GURN was established by the Geodetic Institute (GIK) of Karlsruhe Institute of Technology, Germany, and the École et Observatoire des Sciences de la Terre of University of Strasbourg and French National Center for Scientific Research. Currently, GURN consists of ground-based GNSS stations from permanent authoritative and private GNSS networks. In Germany, this refers to SAPOS

https://doi.org/10.5194/essd-2022-57
Preprint. Discussion started: 7 June 2022

(operated and maintained by the mapping agencies of the German federal states) and GREF (in the responsibility of BKG). In France, the respective networks (in brackets: providers) are RENAG (CNRS) and RGP (IGN) as well as the GNSS networks of the providers TERIA and SAT-INFO. In Switzerland, data from the permanent GNSS network of the federal mapping agency Swisstopo is used. Several stations from IGS and EUREF are also included. For the availability of the raw GNSS observations, readers are referred to the data providers' specific policies. Up to now, only GPS observations have been processed. Other GNSS systems like GLONASS and Galileo will be added in the future.

The GPS data were processed with the GAMIT software (Version 10.7, Herring et al., 2018) for all InSAR dates and for the four seasonal investigation periods. To model the tropospheric delays of GPS signals received by the ground-based stations, we adopted the following equation to map the slant signals into zenith:

$$\begin{aligned} STD(a,e) &= ZHD \cdot mf_H(e) \\ &\quad + ZWD \cdot mf_W(e) + grad(a,e) \end{aligned} \tag{1}$$

$$ZTD = ZHD + ZWD \tag{2}$$

with the corresponding mapping functions mf_H and mf_W; $grad$ is a function to model the effects of azimuthal asymmetry in the tropospheric delays; and a and e are the azimuth and elevation angles of the GPS signals, respectively.

In this study, we used the a priori zenith hydrostatic delay from European Centre for Medium-Range Weather Forecasts (ECMWF; Simmons and Gibson, 2000), the state-of-the-art Vienna Mapping Function 1 (VMF1; Boehm et al., 2006) provided by the Vienna University of Technology, and the tropospheric gradient model proposed by Chen and Herring (1997). Moreover, we conducted the GPS data processing also with other advanced strategies and models. For example, we removed the first-order effect of ionospheric delay with linear combinations of observations and modeled its second- and third-order effects with International Geomagnetic Reference Field 12 (IGRF12; Thébault et al., 2015) and ionospheric data from the Centre for Orbit Determination in Europe (CODE; Schaer, 1999). We removed the observations with elevation angles lower than 10° and weighted the other observations according to their elevation angle and their post-fit phase residuals. We modeled and corrected solid Earth tides, ocean tides, and pole tides according to IERS Conventions 2010 (Petit and Luzum, 2010). We used the IGS final orbits, IGS absolute antenna phase center models (Schmid et al., 2016), and ITRF2014 reference frame (Altamimi et al., 2016).

The tropospheric products derived by the GPS data processing include ZTD, gradients in the north/south and east/west directions, and their corresponding standard deviations, respectively. The ZTD estimates were further used for the retrieval of IWV, with auxiliary information (i.e., P_s and T_m) obtained from ERA5 pressure level products. Detailed procedures for the IWV retrieval from ground-based GPS are provided in the App. A1.

The GPS tropospheric outputs for all the stations, auxiliary variables from ERA5, and the retrieved IWV are saved day by day in ASCII files in solution (software/technique) independent exchange format for tropospheric and meteorological variables Version 2.00 (SINEX-TRO V2.00). The SINEX-TRO V2.00 format was designed to accommodate related developments. For example, it supports tropospheric variables derived by numerical weather prediction models and reanalyses, in addition to space geodetic techniques. The SINEX-TRO V2.00 file is composed of groups of data termed as blocks. Each block has a specific format. Some of the blocks are mandatory (e.g., reference block) whereas the others are optional (e.g., comment line). Thus, the structure of SINEX-TRO V2.00 format is very simple and flexible. For the details on the definition of SINEX-TRO V2.00 format, readers are referred to Pacione and Douša (2017).

The filenames of the GPS tropospheric products are with a style of ‘gikyrdoy0.txt’, where gik is the name of the data provider, yr and doy are year in two characters and day-of-year in three characters, respectively. The files start with metadata blocks and end with data blocks. The metadata blocks include information on data providers, data processing strategies and models, stations’ name, coordinates, receiver types, antenna types and eccentricities, and so on. The data blocks list the GPS-derived ZTD, gradients, and their corresponding standard deviations, respectively. In addition, the data blocks also include the P_s, ZHD, and T_m from ERA5 as well as the final ZWD and IWV estimates.

3.3 InSAR derived ddSTDP and IWV

For deriving double differential slant total delays in phases values (ddSTDP) and IWV from PSI, we use Sentinel-1A/B data, acquired at an altitude of around 690 km in Interferometric Wide Swath Mode (IW) with a ground resolution of around 5 x 20 m and a swath width of 250 km. The data was recorded by both satellites (A,B) along ascending orbit 88 between March 2015 and July 2019. All available datasets are shown in Figure S4 over the time and indicating the along-track coverage in latitude. Each scene is displayed in a different color with additional labels for the four study events. The satellites repeat cylce is 12 days, combining data from both satellites nominally provides an acquisition every 6th day since the launch of Sentinel-1B in October 2016. The acquisition time, 17:26 UTC, is constant for both satellites. With the given repeat cycle of the two satellites 213 scenes could be available theoretically. But some gaps occur in the dataset at certain time intervals, when the project area was not covered for different reasons, leading to the finally processed 169 scenes. In this study, we processed the VV polarized data and used the SRTM-1 as reference digital elevation model during processing. The orbit correction was performed with the provided precise orbit files.

The InSAR processing was performed using the software SNAP, starting with version 7.0 and from the coregistration step onward with version 8.0 (SNAP, 2021). For further PS processing, we then used the program StaMPS (version 4.1-beta, Hooper et al., 2012) for the PSI processing. The master scene for the interferometric processing is from March 17, 2017. The spatial reference point was chosen at the town of Épinal at [6.45066°E, 48.175043°N] with a reference radius of 1 km. Such, we obtain an intermediate dataset of raw double differential slant total delays (ddSTDP) for each interferogram and each PS, which is provided in the dataset publication in the common StaMPS format. Afterwards we estimated the linear displacement at each PS point with a weighted ensemble estimation and removed the displacement phase from the observations. The resulting corrected partial differential slant phase delays (pSWD) are used for the tomographic approach. They are then mapped to zenith direction using the sine function:

$$pZWD_i = pSWD_i * sin(\psi); \quad (3)$$

with the looking angle ψ and the partial wet delays in slant and zenith (pSWD and pZWD) direction. Those corrected phase observations in zenith direction were then used as input into the Atmospheric Phase Screen (APS) inversion. It is based on the zero-mean assumption and is performed point-wise for each PS point independently. The zero-mean assumption does not consider the different heights of PS points. This results in a systematically different behavior of different PS points due to the stratification of the water vapor in the atmosphere. Therefore, we refer to these values as partial Zenith Wet Delays (pZWD). The bias induced through the zero-mean assumption is corrected point-wise using reference values extracted from the ERA5 reanalysis (ECMWF, 2020) to ensure a datum adjustment to the true mean wet delay. The calculation of the required ZWD and mean temperature (T_m) was performed analogously to that described in the GNSS processing section (3.2) and in App. A1.

PSI pZWD contains signal components with long wavelengths which can be biased by several reasons. Therefore, spatial trends over the whole imaged region were re-estimated in the next step. To include only the atmospheric signal, a quadratic function $f(\phi,\lambda)$, as in Equation 4, was estimated which describes the difference between pZWD derived from the ERA5 dataset and the PS-InSAR mean-corrected data. This function depends on geographic longitude λ and latitude ϕ. The estimation parameters a, b, c, d and e differ for each of the 169 scenes.

$$f(\phi,\lambda) = a\cdot\phi^2 + b\cdot\lambda^2 + c\cdot\phi + d\cdot\lambda + e \tag{4}$$

The optimal function is determined using a bootstrapping approach. This approach uses several small subsets of all available PS points to reliably calculate the optimal function (Efron, 1979). The ZWDs were then calculated using the optimal function to correct the mean-corrected ZWDs. Subsequently, the ZWDs were transformed to IWV according to Equation A4.

Finally, we derive the IWV for each PS-point, which is corrected for height errors and includes long wavelength atmospheric signals. The precision of the IWV is estimated for a given PS point as standard deviation of all points located in a 200 m radius w.r.t to this point. The inner precision of the IWV dataset is 0.27 kg/m², which is the average value over all PS points.

The two products provided in the data compilation, each for all 169 dates and at the PS points location, are 1) the double differential slant total phase delays (ddSTDP) at all PS points, and 2) the integrated water vapor (IWV). A potential application of these products is the improvement of methods for gridding and calculation of APS to IWV. The second product can be used for assimilation purposes in weather models.

3.4 WRF-based dynamical downscaling and data assimilation for IWV and WVD

Convection permitting WRF simulations with hourly output were performed for each of the four seasonal study events on the basis of hourly ERA5 driving data (Hersbach et al., 2020). The choice of model physics (see Table 1) is widely adopted from another study in the same region by Wagner et al. (2018) and outlined in more detail in Wagner et al. (2022).

The domain encompasses an area of approximately 650 x 670 km with a grid spacing of 2.1 km and 72 vertical levels (created automatically by WRF). This domain size should guarantee spatial spinup. The temporal spinup is based on several weeks of open cycle simulations before each event to achieve satisfying soil conditions. Open cycle simulations are WRF simulations with hourly ERA5 input but no assimilation of additional variables. In this way reliable starting conditions for the assimilation comparisons were obtained. We performed three simulation runs for each of our chosen events. Run1 is based on the

https://doi.org/10.5194/essd-2022-57
Preprint. Discussion started: 7 June 2022

Table 1. WRF setup and settings.

compartment	scheme
longwave radiation	RRTM (Mlawer et al., 1997)
shortwave radiation	Dudhia (Dudhia, 1989)
microphysics	WSM6 (Hong and Lim, 2006)
planetary boundary layer	YSU (Hong et al., 2006)
convection parametrization	-

assimilation of meteorological stations, GNSS and InSAR data. For Run2 meteorological station data and tomography data was used and Run3 is an open cycle simulation. The 3D-Var technique which is implemented in WRFDA, was applied for the assimilation runs. The multivariate background error statistics option "cv6" was chosen (Barker et al., 2004). In this way, temperature is also able to show a direct impact on moisture and vice versa. A spatial thinning of 10 km was used to minimize correlation artifacts. All assimilation input data except InSAR data was assimilated on an hourly basis. Temperature, pressure and relative humidity from meteorological stations was used along with ZTDs from GNSS, InSAR and interpolated fields by means of collocation. The tomography data is based on the same GNSS data as Run1, but offers gridded input on the WRF grid. The calculation of the ZTD values from GNSS stations and tomography is explained in the respective chapters. ZWD data was provided from InSAR measurements. The dry signal part (ZHD) was calculated from the respective WRF open cycle simulation and was added to the InSAR ZWDs in order to achieve ZTD values for assimilation.

The applied solvers, model time steps and other simulation parameters in WRF are defined in a table called *namelist.input*. This file is included in the dataset as well as a netCDF file called *geo_em.d01.nc*. It contains all static fields in 2D or 3D for the WRF model in the chosen projection, such as altitude, land use, soil information etc. Additionally, the background error covariance matrix *(be.dat)* is required for the assimilation. It was calculated with the NMC-method (Parrish and Derber, 1992) for each of our events. Based on month-long WRF simulations with the same setup as our open cycle simulations, averaged forecast differences of the 12 hour and 24 hour forecast (valid at the same time) were applied. Furthermore, the assimilation input for Run1 is provided (obsproc_hour). This is a pre-processed input where observation errors were included and duplicates and inconsistence data due to certain tests were removed. For raw assimilation data we refer to the other datasets presented in Section 3. The meteorological station data is available at DWD (DWD, 2020). Our forcing data ERA5 can be obtained from the ECMWF website (ECMWF, 2020).

WRF output is available on the 3D model grid. The direct nesting from 31 km to 2.1 km reduces possible artifacts due to intermediate domains and the respective parametrizations (e.g., convection) on one hand. On the other hand, model physics requires a larger area to evolve. That is why we discarded an area of 50 pixels at the borders to achieve reliable simulation outcomes. The results are provided after 1 hour free WRF simulations to obtain consistent model data, since the assimilation of variables modifies only certain model variables. Temperature, pressure, and water volume density are provided on a 3D grid (219 x 209 x 72). In 2D, temperature and pressure are provided in 2 meters and Integrated Water Vapor (IWV) and rain amounts as column values.

https://doi.org/10.5194/essd-2022-57
Preprint. Discussion started: 7 June 2022

3.5 Tomography derived ZTD, refractivity, and WVD

The least squares collocation approach is based on a functional and a stochastic component where correlated parts are determined and separated from uncorrelated measurement noise (for instance from Eckert et al., 1992a):

$$l = f(u,x,t) + s(C_{ss},x,t) + \epsilon \tag{5}$$

where l is the measurement, $f(u,x,t)$ the functional part, representing 'realistic' physical models of meteorological variables with u, x and t respectively the state vector to be estimated, the coordinates and the time. The so-called signal $s(C_{ss},x,t)$ depends on an empirically modeled covariance C_{ss}, and the noise ϵ is assumed as stochastically uncorrelated.

In our collocation software, the state vector to be estimated is $u = (ZTD_0, a_{ZTD}, b_{ZTD}, c_{ZTD}, H_{ZTD})$; ZTD_0 is the ZTD at reference position (x_0, y_0, h_0, t_0), a_{ZTD}, b_{ZTD}, c_{ZTD} are gradients in the x,y coordinate and time, and H_{ZTD} the scale height. x,y,h,t represent the coordinates and time of a measured point. MFs are mapping functions used to map zenith delays in the slant direction. Thus, according to Hurter (2014) and Shehaj et al. (2020), the ZTDs and $ddSTD$s are modeled as follows:

$$\begin{aligned} ZTD(x,y,h,t) = {} & [ZTD_0 + a_{ZTD}\cdot(x-x_0) \\ & + b_{ZTD}\cdot(y-y_0) + c_{ZTD}\cdot(t-t_0)] \\ & \cdot e^{-\frac{h-h_0}{H_{ZTD}}} \end{aligned} \tag{6}$$

$$\begin{aligned} ddSTD(x,y,h,t) = {} & [MF_{p1}^{t1}\cdot ZTD_{p1}^{t1} \\ & - MF_{p_{ref}}^{t1}\cdot ZTD_{p_{ref}}^{t1}] \\ & - [MF_{p1}^{t_{ref}}\cdot ZTD_{p1}^{t_{ref}} \\ & - MF_{p_{ref}}^{t_{ref}}\cdot ZTD_{p_{ref}}^{t_{ref}}] \end{aligned} \tag{7}$$

For the $ddSTD$, the superscripts $t1, t_{ref}$ represent the time of acquisition of an InSAR image and the reference image acquisition time, forming the time difference, while the subscripts $p1, p_{ref}$ refer to the positions of an InSAR PS point in the image and the position of the reference PS point forming the spatial difference. The formulas describing the covariance of the signal part can be found in Eckert et al. (1992a) and Eckert et al. (1992b).

For the collocation of GNSS and InSAR measurements two steps are required: 1) Screening of GNSS ZTDs and InSAR $ddSTD$s, based on simple least squares estimation and gross error detection. The value of the residuals divided by the product of the a posteriori standard deviation and measurement noise is compared to a preselected threshold. 2) least squares collocation of the measurements passing the screening process. The signal and the noise of each measurement are defined respectively by the covariance of the signal C_{ss} and the covariance of the noise (which is a diagonal matrix describing the variance of each measurement).

The refractivity (N) equals the derivative of the delay in the direction of the ray. Thus, by deriving the zenith delays with respect to height we obtain:

$$N(x,y,h,t) = -\frac{\partial ZTD(x,y,h,t)}{\partial h} \tag{8}$$

$$\begin{aligned} N(x,y,h,t) = {} & \frac{1}{H_{ZTD}} \cdot [ZTD_0 + a_{ZTD} \cdot (x - x_0) \\ & + b_{ZTD} \cdot (y - y_0) + c_{ZTD} \cdot (t - t_0)] \\ & \cdot e^{-\frac{h-h_0}{H_{ZTD}}} \end{aligned} \tag{9}$$

The covariance matrices relating delays with refractivity, as shown in Hurter (2014), are obtained by deriving the covariance of the delays with respect to height.

Two kind of products are provided in this study: 1) 2D maps of ZTDs interpolated onto the grid of the WRF domain (Sec. 3.4), which contain structural information of the lowest tropospheric layer and 2) 3D *tomographic* products in form of refractivity fields on the horizontal grid of the WRF domain; for the vertical distribution the refractivities are computed for 16 equally distributed layers, from the lowest WRF layer up to 8 km.

Examples of ZTDs and refractivity fields, obtained using our approach, are shown in Fig. 4 for the spring event of 2016. From the top plot in Fig. 4 it can be noticed that the ZTDs and the refractivity fields for the lowest layer follow the topography of the terrain, whilst in bottom plot the decrease in refractivity with altitude is visible.

A further, extended time series of tomographic products is provided based on the InSAR and GNSS collocated tropospheric products, described in section 3.2 and section 3.3. The length of the time series corresponds to the number of InSAR acquisitions, since the scope is to exploit the two techniques simultaneously. Therefore, the temporal resolution is similar to that of the InSAR products, while the spatial resolution of these products is identical to the 2D maps of ZTDs or 3D fields of refractivity described above.

For the four seasonal events (Sec. 3), the 2D maps of ZTDs were stored as ASCII files, where each line corresponds to one epoch and the number of columns to the number of points in the horizontal grid of the WRF model. For the 3D tomographic products the structure is identical, however the number of columns is 16 times larger since there are 16 layers. For each WRF point, the 16 refractivity values are written and then going to the next point until the last one.

Potential applications of our data are the fusion in numerical weather prediction models as well as use of retrieved ZTDs and refractivities for validation purposes. Regarding the retrieval of IWV and WVD fields, more information is provided in the Appendix.

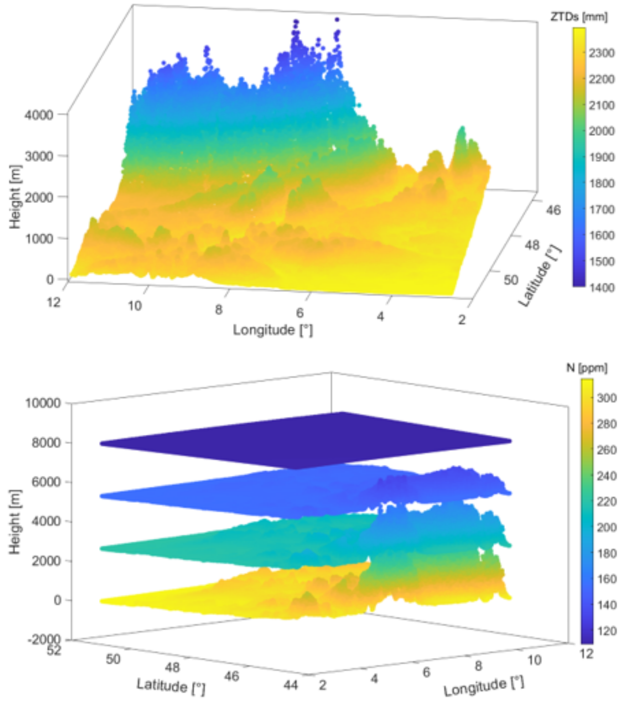

Figure 4. Fields of collocated (top) GNSS ZTDs and (bottom) refractivities.

4 Data evaluation and cross comparison

To examine the quality of the developed products with respect to IWV, the datasets are evaluated with independent observations and jack-knife cross validation at five representative GNSS stations (cyan dots in Fig. 2) of the study region. The Kling-Gupta efficiency measure (KGE, Gupta et al., 2009) is used to evaluate coherence among the time series of the different products (a and b):

$$KGE = 1 - \sqrt{(r-1)^2 + (\alpha - 1)^2 + (\beta - 1)^2} \tag{10}$$

with the correlation coefficient r, the relative variability $\alpha = \sigma_a / \sigma_b$ (the ratio of standard deviations), and the bias ratio $\beta = \mu_a / \mu_b$.

The 1-hourly GNSS-derived ZTD and IWV time series for the 66 GURN stations are compared to the estimates obtained from ERA5 pressure level products from 2015 to 2019 as shown in Tab. 2. Quite good agreement is obtained, with mean KGE values of 0.98 and 0.97 for the ZTD and IWV, respectively. In addition, we validate the GNSS results with respect to nearby radiosonde measurements at 00 and 12 UTC for the same period. The radiosonde data is derived from the Integrated Global Radiosonde Archive (IGRA) Version 2. We determine a GNSS and radiosonde station pair if their horizontal distance is within

Table 2. Performance measures for GNSS derived ZTD and IWV time series with respect to ERA5 (GNSS-ERA5, 66 GURN stations) and radiosonde (GNSS RS, 4 stations) data.

		β	α	r	KGE
GNSS-ERA5	ZTD	1.00	1.00	0.98	0.98
	IWV	0.98	1.00	0.98	0.97
GNSS-RS	ZTD	0.99	1.00	0.98	0.97
	IWV	0.99	1.00	0.98	0.97

50 km and their height difference is within 100 m. Four station pairs are then determined, namely 0384-GMM00010739, 0389-GMM00010739, 0400-GMM00010739, and BIRK-GMM00010618. For each station pair, the radiosonde ZTD and IWV are calculated by using integration of vertical profiles from the corresponding GNSS station height. The mean KGE values (0.97) for the GNSS-derived ZTD and IWV with respect to the corresponding radiosonde results are also very high (Tab. 2).

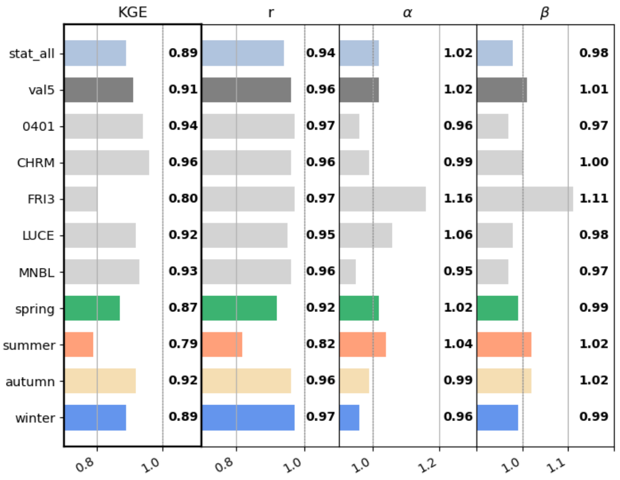

Figure 5. Performance measures for IWV of PS-InSAR vs. GNSS for different station subsets within the InSAR domain (all stations, validation stations, single stations, and seasons).

The InSAR-derived IWV results are compared to the GNSS-derived IWV at the GNSS stations. Firstly, the ten nearest InSAR PS-points to the GNSS stations are computed and a height correction based on ERA5-IWV standard atmospheric height dependencies is applied. 25 GNSS stations are located within the InSAR domain and have sufficient data points. Fig. 5 shows the KGE and its constituents for different subsets of the data. The mean values of the KGE over all 25 GNSS stations in the SAR area are presented on top, followed by the mean over the 5 validation stations, with superior agreement of the latter. The detailed description for each validation station are displayed separately with the worst performance at station FRI3. At the bottom of the figure, the validation stations data are split into the different seasons, independent of the year, and validated separately. The best results are obtained in autumn, followed by winter and spring, whereas the summer shows the highest differences.

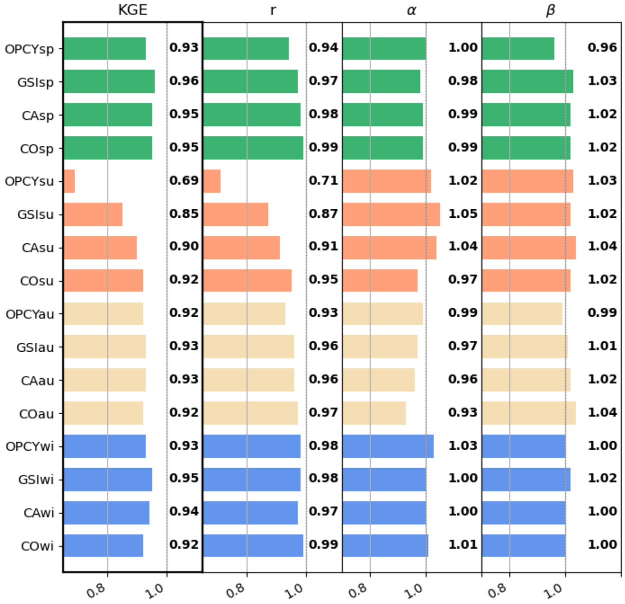

Figure 6. Performance measures for IWV of WRF simulations and original tomography collocation data (CO) vs. 5 GNSS validation stations. The abbreviations represent the assimilated observations: e.g., OPCY = open cycle, GSI = GNSS, synoptic and InSAR data, CA = collocation data and the seasons spring, summer, autumn, winter (sp,su,au,wi).

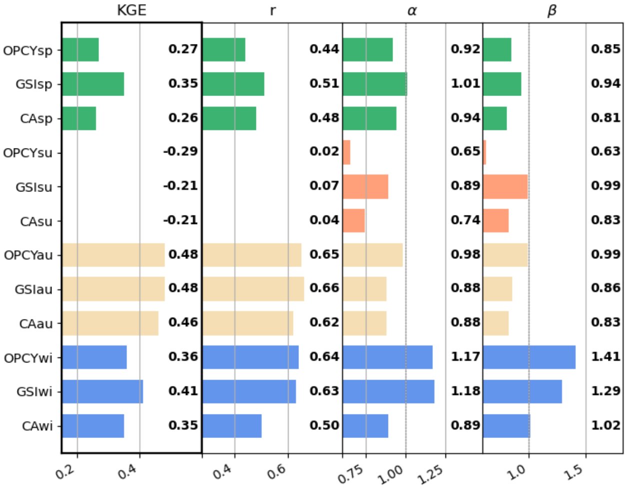

Figure 7. Same as Fig. 6 but for precipitation amounts at approx. 350 stations and only for the WRF simulations.

WRF simulation results are compared to 5 GNSS stations for IWV (Fig. 6) and to 350 stations for precipitation amounts (Fig. 7) for each of the four events. Fig. 6 reveals that a high accordance between GNSS stations and the open cycle simulations already exist for spring, autumn and winter with KGE values of approximately 0.93 for IWV. Only in summer the KGE value is below 0.7 due to convective activity. Despite the already high accordances, slight improvements for all seasons are obtained by assimilation of tomography data (CA) as well as by assimilation of station data (GSI). This is most evident in summer with KGEs now larger than 0.85. Original collocation data (CO) shows the best performance regarding correlation for all seasons. The KGE of CO is only best in summer, but there is still a high accordance for the other seasons, similar to the assimilation runs.

A similar picture is obtained for precipitation (Fig. 7), however with much lower KGE values. The best agreement for the open cycle simulations is obtained in autumn, the worst again in summer. The assimilation of ZTD only (CA) improved only the simulation results in summer. But for the joint assimilation of water vapor values and temperature data (GSI), an improvement for every season becomes obvious.

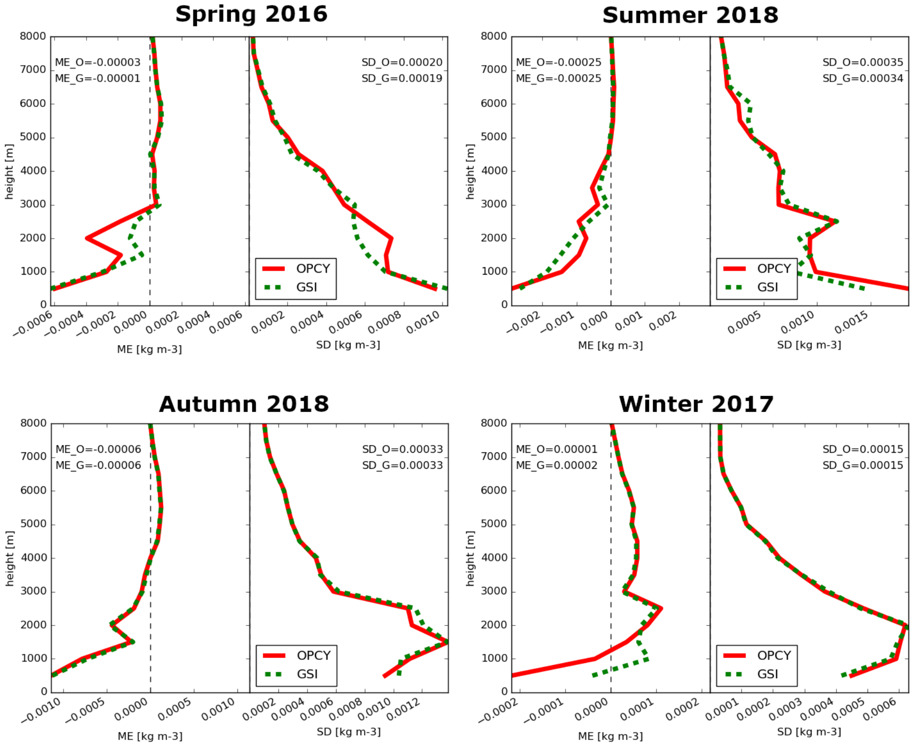

Figure 8. Mean error (ME) and standard deviation (SD) of the water vapor density for all seasons, comparing the simulations with open cycle (red) and the assimilation of station data (green) with radiosonde data for the location of Idar-Oberstein (X-axis range varies for the different seasons).

The vertical distribution of water vapor is evaluated based on profiles of water vapor density (WVD; Sec. A3) with respect to radiosonde observations. In Fig. 8, the mean profiles of WVD from simulation results are opposed to radiosonde data for Idar-Oberstein. The results for IWV and precipitation are likewise for the vertical distribution. In autumn, there are hardly any differences between OPCY and simulations with assimilation, while improvements can be seen in the other seasons. In winter, differences become clear up to a maximum of 2500 m; but mainly only up to an altitude of 1500 m. In spring and especially in summer, however, there are also differences above an altitude of 4000 m. Improvements through assimilation are not uniform for every altitude in every season. But on average, the results for the simulations with assimilation show a better performance in terms of mean error and standard deviation than without.

A cross validation between the GNSS derived IWVs and collocated/interpolated ones using COMEDIE is shown in Fig. 9, where the reference IWVs are shown in continuous lines and the ones collocated in dashed lines. These 5 stations were not used in the collocation process to derive the parameters that define the functional part of the collocation, therefore the GNSS and COMEDIE derived IWVs can been treated as independent. At a first glance, the continuous and dashed curves in Fig. 9 seem to follow a similar pattern. However, from the differences in Fig. 10 we can see that there are some millimeter differences for all five stations for all the events. At humid days and during periods of high IWV variability a bigger disagreement is obtained and smallest differences occur in the winter season. The statistics (mean value and standard deviation) for each station are always below 1 mm for winter, spring and autumn events, however only for the summer events the standard deviation of the differences is around 1 mm. On the one hand this evaluation shows the capabilities of our collocation method to interpolate GNSS dervied IWVs. On the other hand it is a mean to check the internal consistency of GNSS dervied IWVs of the GURN network.

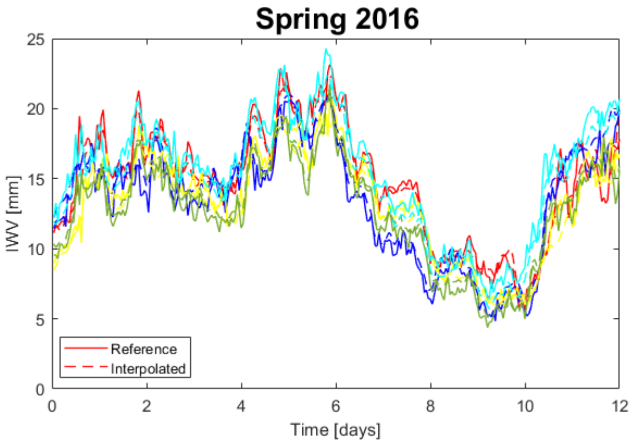

Figure 9. Interpolated vs. reference GNSS estimated IWV at 5 validation stations.

In Fig. 11, we compare IWV fields between WRF (open cycle simulation) and COMEDIE for the events in Spring 2016, where the differences for one epoch (top panel) and the averaged differences (bottom panel) for all epochs are shown. For every epoch there are a few millimeters differences depending on the pixel (with overall standard deviation at sub-millimeter

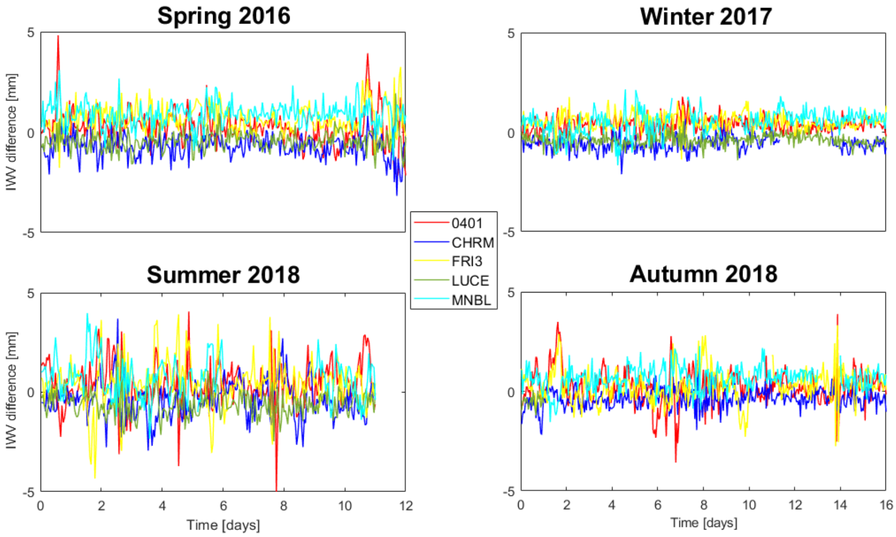

Figure 10. Residuals between GNSS estimated and collocated IWV at 5 validation stations.

level), whilst in the bottom plot the difference is smoothed, with an even smaller standard deviation over all epochs and pixels. Furthermore, it is interesting to notice that the differences are not notably larger in the lower-right corner of the grid where the mountainous area is located meaning the differences between WRF and COMEDIE are not topographically related.

5 Conclusions

The dataset developed and presented in this work provides a comprehensive, multi-perspective, multi-season, and multi-scale observation of tropospheric water vapor over the study area in the transborder region of Germany, Switzerland, and France. GNSS derived IWV is highly accurate and features high temporal resolution, whereas the InSAR products score with their spatial density. The combination of both by collocation or tomography and the assimilation with regional atmospheric models yields sophisticated descriptions of tropospheric moisture states that cannot be derived from the individual methods alone. The ECMWF ERA5 global reanalysis depicts a valuable resource for the GNSS based determination of ZWD and IWV for stations with lacking meteorological observations and likewise for the computation from InSAR. The limited area WRF simulations for the GURN region benefited from the assimilation of either GNSS, synoptic, InSAR, and collocation data, with the latter leading to slightly inferior results. The strongest impact is seen for the summer event where levels of IWV are generally high and fluctuations are strong because of convective dynamics. The joint assimilation of water vapor and temperature yields in particular a largely better performance of GSI compared to CA.

The presented dataset will be useful for all kind of studies that require high resolution information about tropospheric water vapor states and -dynamics. In future studies the spatial coverage could be increased to continental scale extent to study the impact of tropospheric water vapor assimilation on the larger scale. Other GNSS systems such as Galileo or GLONASS could

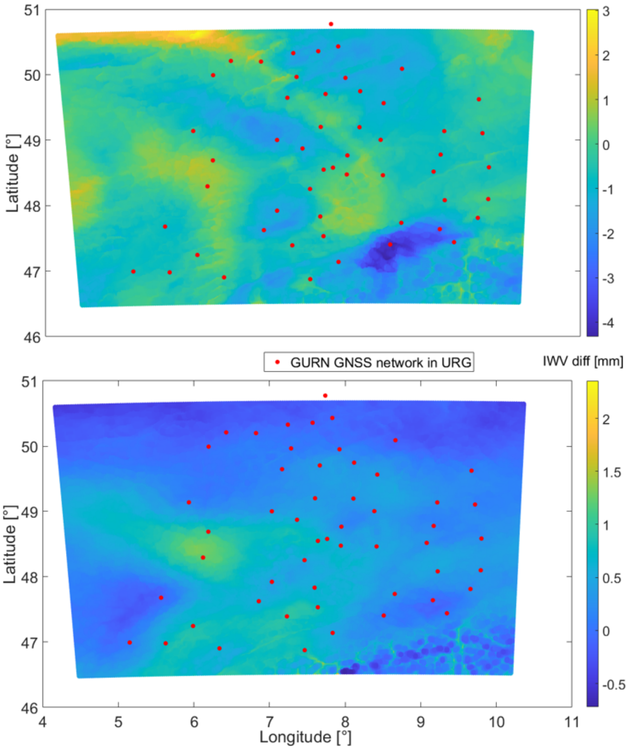

Figure 11. Differences between collocated IWVs and WRF model (open cycle simulation) for Spring 2016. In the top subplot, one epoch (epoch 1) is displayed, whilst in the bottom plot the mean over all epochs is shown.

also be included to provide more observations. The new generation of currently realized microsatellite missions like Capella X-SAR will significantly increase the temporal sampling of InSAR derived tropospheric water vapor products from several days currently to less than one hour in future. This will further increase the relevance of InSAR. Finally, the beneficial joint assimilation of energy quantities can be extended by radiation products. Other dataset, such as GNSS radio occulations can be included into the combination, which can provide complementary information regarding water vapor in the higher troposphere.

6 Code and data availability

The dataset described in this paper was published on the PANGEA data publishing platform under (https://www.pangaea.de/tok/e11e2f371fb3b638563ed6b6e3128564ba9ba845, Fersch et al., 2021). The ERA5 global atmospheric reanalysis data is available at the Copernicus Climate Data service of the European Union (https://climate.copernicus.eu/climate-reanalysis: last access 4 January, 2022). The WRF model code can be obtained from GitHub (https://github.com/wrf-model/WRF: last access. 4 January, 2022).

The GAMIT GNSS data processing software can be obtained from (http://geoweb.mit.edu/gg/: last access 4 January, 2022). The Sentinel data are freely available through the Copernicus program (Copernicus, 2020). The COMEDIE software routines can be made available on request and after approval of ETH Zurich. However, all the formulations and implementations have been described in (Eckert et al., 1992a, b; Hurter, 2004, 2014).

Appendix A: Conversion and computation details

A1 Computation of ZWD and IWV with T_m, P_s from ERA5 reanalysis

In order to retrieve IWV from GPS-derived ZTD, we firstly determine the four grid nodes surrounding the GPS station horizontally. We then calculate the related variables (e.g., P_s) of the grid nodes at the station's height. Finally, we calculate the IWV at the station's location by using inverse distance weighting (IDW) interpolation (Jade and Vijayan, 2008). For each grid node, we calculate ZHD according to the Saastamoinen model (Saastamoinen, 1972):

$$ZHD = \frac{2.2768 \cdot P_s}{1 - 2.66 \times 10^{-3} \cdot \cos(2\phi_s) - 2.8 \times 10^{-7} \cdot h_s} \tag{A1}$$

where P_s is the pressure at the GPS station obtained from reanalysis products, ϕ_s and h_s are the stations' latitude and its height above the geoid, respectively. In this process, the barometric correction formula recommended by the International Civil Aviation Organization (ICAO) is applied:

$$P_s = P_0 \cdot (1 - \frac{\gamma}{T_0}(h_s - h_0))^{\frac{g_0}{\gamma \cdot R_d}} \tag{A2}$$

where P_0 is the referential pressures with a height of h_0, T_0 is the temperature in K at the height of h_0, γ=0.0065 K m^{-1} is the standard temperature lapse rate, g_0=9.80665 m s^{-2} is the standard acceleration of gravity, and R_d=287.033 J kg^{-1} K^{-1} is the gas constant for dry air. Then, we obtain ZWD given by:

$$ZWD = ZTD - ZHD \tag{A3}$$

Finally, we convert the ZWD into IWV (Bevis et al., 1994):

$$IWV = \frac{10^6 \cdot ZWD}{\rho \cdot Rw \cdot (k_{21} + \frac{k_3}{T_m})} \tag{A4}$$

where ρ=1000 kg m^{-3}, Rw=461.522 J kg^{-1} K^{-1}, k_{21}=22.1 K hPa^{-1}, k_3=373900 K^2 hPa^{-1}. T_m is the weighted mean temperature given by (Davis et al., 1985):

$$T_m = \frac{\int \frac{e}{T} \mathrm{d}h}{\int \frac{e}{T^2} \mathrm{d}h} \tag{A5}$$

The vapor pressure is given by:

$$e = e_{sat}(T) \cdot RH \tag{A6}$$

whereas $e_{sat}(T)$ and RH denote saturation vapor pressure and relative humidity, respectively. The saturation vapor pressure is estimated using Tetens's formula (IFS CY41R2):

$$e_{sat}(T) = a_1 \cdot \exp(a_3 \frac{T - T_0}{T - a_4}) \tag{A7}$$

where a_1 = 611.21 Pa and T_0 = 273.16 K, a_3 = 17.502, and a_4 = 32.19 K for saturation over water. For the saturation over ice, a_3 = 22.587 and a_4 =-0.7 K. As the T_m is integrated from GPS station height to the highest reanalysis level, the RH and temperature at the station are calculated with linear inter-/extra-polation.

In addition, to assist the estimation of InSAR-derived ZWD, the ZWD obtained from ERA5 pressure level products are calculated:

$$ZWD = 10^{-6} \int N_w \, \mathrm{d}h \tag{A8}$$

where N_w is the wet component of refractivity (Davis et al., 1985):

$$N_w = k_2 \frac{e}{T} + k_3 \frac{e}{T^2} \tag{A9}$$

Likewise, the ERA5 derived ZTD and IWV in meters can be calculated as follows:

$$ZTD = 10^{-6} \int N \, \mathrm{d}h \tag{A10}$$

where N is the refractivity (Davis et al., 1985):

$$N = k_1 \frac{p_d}{T} + k_2 \frac{e}{T} + k_3 \frac{e}{T^2} \tag{A11}$$

k_3=373900 K^2 hPa^{-1} and p_d is the pressure of dry air.

$$IWV = \int \rho_w \, \mathrm{d}h \tag{A12}$$

where ρ_w is the density of water vapor and k_1=77.6 K hPa^{-1}, k_2=70.4 K hPa^{-1} and k_3=373900 K^2 hPa^{-1}

A2 Computation of water vapor density from collocated IWV

For the retrieval of IWV fields using COMEDIE, we have separately performed collocation/interpolation of zenith total delays and zenith dry delays and thus computed zenith wet delays as their differences. Using Tm from ERA-5, we have obtained the final IWV fields displayed in this paper here.

The retrieval of water vapor density fields has been performed similarly to the retrieval of refractivity fields from ZTDs described in Sec. 3.5, where in Eq. 6 and Eq. 9 ZTDs and refractivities were replaced by IWVs and WVDs, respectively.

A3 Computation of IWV and WVD from WRF data

The integrated water vapor and the water vapor density from WRF is calculated based on the water vapor mixing-ratio, temperature and pressure for the 72 vertical pressure levels. Temperature T is defined as:

$$T = (T_P + T_{base}) \cdot P^{\frac{R_D}{cp}} \tag{A13}$$

https://doi.org/10.5194/essd-2022-57
Preprint. Discussion started: 7 June 2022

where T_P is the potential perturbation, T_{base} = 300 K is the base temperature, P is the pressure, R_D=287 J kg^{-1} K^{-1} is the gas constant for dry air and cp = 1004.5 J kg^{-1} K^{-1} is heat capacity at constant pressure for dry air.

The integrated water vapor is calculated as the sum of water vapor in the vertical levels:

$$IWV = \sum \frac{Q_V \cdot dh \cdot P}{R_D \cdot T_V} \tag{A14}$$

where Q_V is the water vapor mixing ratio, dh is the layer thickness and T_V is the virtual temperature of each level. With:

$$T_V = \frac{T \cdot \epsilon + Q_V}{\epsilon \cdot (1 + Q_V)} \tag{A15}$$

where ϵ is the ratio of the gas constants of air and water vapor = 0.622.

The three-dimensional water vapor density is calculated as follows:

$$WVD = \frac{Q_V \cdot P}{R_D \cdot T} \tag{A16}$$

Appendix B: Abbreviations

Term	Abbr.	Unit
Atmospheric phase screen	APS	rad
Collocation assimilation	CA	
Collocation data	CO	
Collocation software	COMEDIE	
Double differential slant total delay	ddSTD	mm
Double differential slant total delay phases	ddSTDP	rad
ECMWF reanalysis 5	ERA5	
German Weather Service	DWD	
Global navigation satellite systems	GNSS	
Global positioning system	GPS	
GNSS Upper Rhine Graben Network	GURN	
GNSS, synoptic, and InSAR data assimilation	GSI	
Integrated water vapor	IWV	
Interferometric Synthetic Aperture Radar	InSAR	
Kling-Gupta efficiency metric	KGE	-
Limited area model	LAM	
Line of sight	LOS	
Mapping function	MF	
Open cycle simulation	OPCY	
partial slant wet delay	pSWD	mm
partial zenith wet delay	pZWD	mm
Persistent scatterers	PS	
Persistent scatterers inferometry	PSI	
Refractivity	N	ppm
Slant total delay	STD	mm
Synthetic aperture radar	SAR	
Upper Rhine Graben	URG	

Term	Abbr.	Unit
Water vapor density	WVD	kg m^3
Weather research and forecasting modeling system	WRF	
Data assimilation specialized version WRF	WRFDA	
Zenith delay	ZD	mm
Zenith hydrostatic delay	ZHD	mm
Zenith total delay	ZTD	mm
Zenith wet delay	ZHD	mm

Author contributions. BF conceived the manuscript structure and contributed to all sections. Moreover, BF put together the data collection and organized the publication at Pangaea. PY created the GNSS dataset, wrote the GNSS related parts, and performed the calculations of related variables (e.g., P_s, T_m, ZWD, IWV) from ERA5 reanalysis for the GNSS and InSAR products (Appendix A1). BK created the InSAR derived data products and wrote the InSAR related parts together with AS. ES produced the collocation and tomography datasets and wrote the respective parts with GM. AW performed the data assimilation with WRF, created the respective datasets and authored the corresponding passages. AG, BH, SH, HKun, and HKut contributed to the conception and design of the study. All authors contributed to the writing of the general parts of the manuscript.

Competing interests. The authors declare that they have no conflict of interest.

Acknowledgements. We would like to thank EOST (École et Observatoire des Sciences de la Terre of University of Strasbourg and French National Center for Scientific Research, France) for the collaborations on maintaining the GURN network. Thanks are also given to the GNSS data providers, such as SAPOS (AdV) and GREF (BKG) from Germany, RENAG (CNRS), TERIA, RGP (IGN), and SAT-INFO from France, and Swisstopo from Switzerland, and also EPN (EUREF) and IGS. We are also grateful to National Centers for Environmental Information (NCEI) for providing the radiosonde data. We would like to acknowledge the German Meteorological Service (DWD) for supplying us synoptic station data. Furthermore we thank the PANGEA data publisher for its excellent service and their help with processing and hosting the dataset developed in this work.

References

Almansa, A. F., Cuevas, E., Barreto, Á., Torres, B., García, O. E., García, R. D., Velasco-Merino, C., Cachorro, V. E., Berjón, A., Mallorquín, M., López, C., Ramos, R., Guirado-Fuentes, C., Negrillo, R., and de Frutos, Á. M.: Column Integrated Water Vapor and Aerosol Load Characterization with the New ZEN-R52 Radiometer, Remote Sensing, 12, 1424, https://doi.org/10.3390/rs12091424, 2020.

Alshawaf, F., Fersch, B., Hinz, S., Kunstmann, H., Mayer, M., and Meyer, F. J.: Water vapor mapping by fusing InSAR and GNSS remote sensing data and atmospheric simulations, Hydrol. Earth Syst. Sci., 19, 4747–4764, https://doi.org/10.5194/hess-19-4747-2015, 2015a.

Alshawaf, F., Hinz, S., Mayer, M., and Meyer, F. J.: Constructing accurate maps of atmospheric water vapor by combining interferometric synthetic aperture radar and GNSS observations, Journal of Geophysical Research: Atmospheres, 120, 1391–1403, https://doi.org/10.1002/2014JD022419, 2015b.

Alshawaf, F., Zus, F., Balidakis, K., Deng, Z., Hoseini, M., Dick, G., and Wickert, J.: On the statistical significance of climatic trends estimated from GPS tropospheric time series, Journal of Geophysical Research: Atmospheres, 123, 10–967, 2018.

Altamimi, Z., Rebischung, P., Métivier, L., and Collilieux, X.: ITRF2014: A new release of the International Terrestrial Reference Frame modeling nonlinear station motions, Journal of Geophysical Research: Solid Earth, 121, 6109–6131, 2016.

Andersson, E., Hólm, E., Bauer, P., Beljaars, A., Kelly, G. A., McNally, A. P., Simmons, A. J., Thépaut, J.-N., and Tompkins, A. M.: Analysis and forecast impact of the main humidity observing systems, Quarterly Journal of the Royal Meteorological Society, https://doi.org/10.1002/qj.112, 2007.

Barker, D., Huang, W., Guo, Y., and Bourgeois, A.: A Three-demiensional Variational (3DVAR) Data Assimilation System for Use With MM5, Monthly Weather Review - MON WEATHER REV, https://doi.org/10.5065/D6CF9N1J, 2003.

Barker, D., Huang, W., Guo, Y., Bourgeois, A., and Xiao, A.: A Three-Dimensional Variational Data Assimilation System for MM5: Implementation and Initial Results, Monthly Weather Review - MON WEATHER REV, 132, https://doi.org/10.1175/1520-0493(2004)132<0897:ATVDAS>2.0.CO;2, 2004.

Bevis, M., Businger, S., Herring, T. A., Rocken, C., Anthes, R. A., and Ware, R. H.: GPS meteorology: Remote sensing of atmospheric water vapor using the global positioning system, 97, 15 787–15 801, https://doi.org/10.1029/92JD01517, 1992.

Bevis, M., Businger, S., Chiswell, S., Herring, T. A., Anthes, R. A., Rocken, C., and Ware, R. H.: GPS meteorology: Mapping zenith wet delays onto precipitable water, Journal of applied meteorology, 33, 379–386, 1994.

Boehm, J., Werl, B., and Schuh, H.: Troposphere mapping functions for GPS and very long baseline interferometry from European Centre for Medium-Range Weather Forecasts operational analysis data, Journal of geophysical research: solid earth, 111, 2006.

Boniface, K., Ducrocq, V., Jaubert, G., Yan, X., Brousseau, P., Masson, F., Champollion, C., Chery, J., and Doerflinger, E.: Impact of high-resolution data assimilation of GPS zenith delay on Mediterranean heavy rainfall forecasting, Annales Geophysicae, 27, https://doi.org/10.5194/angeo-27-2739-2009, 2009.

Brönnimann, S.: The Basis: Past Climate Observations and Methods, in: Advances in Global Change Research, pp. 9–69, Springer International Publishing, https://doi.org/10.1007/978-3-319-19042-6_2, 2015.

Bähr, H. and Hanssen, R.: Reliable estimation of orbit errors in spaceborne SAR interferometry, Journal of Geodesy, 86, 1147–1164, https://doi.org/10.1007/s00190-012-0571-6, 2012.

Chen, G. and Herring, T.: Effects of atmospheric azimuthal asymmetry on the analysis of space geodetic data, Journal of Geophysical Research: Solid Earth, 102, 20 489–20 502, 1997.

Copernicus: Copernicus Sentinel data [2015-2019], https://scihub.copernicus.eu/, [Online; accessed 22 October 2020], 2020.

Crosetto, M., Monserrat, O., Cuevas-González, M., Devanthéry, N., and Crippa, B.: Persistent Scatterer Interferometry: A review, https://doi.org/10.1016/j.isprsjprs.2015.10.011, 2016.

Davis, J., Herring, T., Shapiro, I., Rogers, A., and Elgered, G.: Geodesy by radio interferometry: Effects of atmospheric modeling errors on estimates of baseline length, Radio science, 20, 1593–1607, 1985.

Dee, D. P., Uppala, S. M., Simmons, A. J., Berrisford, P., Poli, P., Kobayashi, S., Andrae, U., Balmaseda, M. A., Balsamo, G., Bauer, P., Bechtold, P., Beljaars, A. C. M., van de Berg, L., Bidlot, J., Bormann, N., Delsol, C., Dragani, R., Fuentes, M., Geer, A. J., Haimberger, L., Healy, S. B., Hersbach, H., Hólm, E. V., Isaksen, L., Kållberg, P., Köhler, M., Matricardi, M., McNally, A. P., Monge-Sanz, B. M., Morcrette, J.-J., Park, B.-K., Peubey, C., de Rosnay, P., Tavolato, C., Thépaut, J.-N., and Vitart, F.: The ERA-Interim reanalysis: configuration and performance of the data assimilation system, Quarterly Journal of the Royal Meteorological Society, 137, 553–597, https://doi.org/10.1002/qj.828, 2011.

Divakarla, M. G., Barnet, C. D., Goldberg, M. D., McMillin, L. M., Maddy, E., Wolf, W., Zhou, L., and Liu, X.: Validation of Atmospheric Infrared Sounder temperature and water vapor retrievals with matched radiosonde measurements and forecasts, Journal of Geophysical Research, 111, https://doi.org/10.1029/2005JD006116, 2006.

Dudhia, J.: Numericall study of convection observed during the Winterl Monsoonl Experimentl using a mesoscale two–dimensional model, J. Atmos. Sci., 46, 3077–3107, 1989.

DWD: DWD synoptic data, http://www.dwd.de/DE/leistungen/radolan/radolan_info/ radolan_change_management_pdf, https://opendata.dwd.de/climate_environment/CDC/observations_germany, [Online; accessed 4 Decembre 2020], 2020.

Eckert, V., Cocard, M., and Geiger, A.: COMEDIE: (Collocation of meteorological data for interpretation and estimation of tropospheric pathdelays) Teil I: Konzepte, Teil II: Resultate; Technical Report 194, ETH Zürich, [Grauer Bericht], 1992a.

Eckert, V., Cocard, M., and Geiger, A.: COMEDIE: (Collocation of meteorological data for interpretation and estimation of tropospheric pathdelays) Teil III: Software; Technical Report 195, ETH Zürich, [Grauer Bericht], 1992b.

ECMWF: ERA5 reanalysis data, https://www.ecmwf.int/en/forecasts/datasets/reanalysis-datasets/era5, https://www.ecmwf.int/en/forecasts/datasets/reanalysis-datasets/era5, [Online; accessed 4 Decembre 2020], 2020.

Efron, B.: Bootstrap Methods: Another Look at the Jackknife, The Annals of Statistics, 7, 1 – 26, https://doi.org/10.1214/aos/1176344552, 1979.

Feltz, W. F., Smith, W. L., Howell, H. B., Knuteson, R. O., Woolf, H., and Revercomb, H. E.: Near-Continuous Profiling of Temperature, Moisture, and Atmospheric Stability Using the Atmospheric Emitted Radiance Interferometer (AERI), Journal of Applied Meteorology, 42, 584–597, https://doi.org/10.1175/1520-0450(2003)042<0584:npotma>2.0.co;2, 2003.

Ferretti, A., Prati, C., and Rocca, F.: Permanent scatterers in SAR interferometry, IEEE Transactions on Geoscience and Remote Sensing, 39, 8–20, https://doi.org/10.1109/36.898661, 2001.

Fersch, B., Senatore, A., Adler, B., Arnault, J., Mauder, M., Schneider, K., Völksch, I., and Kunstmann, H.: High-resolution fully coupled atmospheric–hydrological modeling: a cross-compartment regional water and energy cycle evaluation, Hydrology and Earth System Sciences, 24, 2457–2481, https://doi.org/10.5194/hess-24-2457-2020, 2020.

Fersch, B., Kamm, B., Shehaj, E., Wagner, A., Yuan, P., Möller, G., Schenk, A., Geiger, A., Hinz, S., Kutterer, H., and Kunstmann, H.: A comprehensive high resolution data collection for tropospheric water vapor assessment for the Upper Rhine Graben, Germany (In review)., https://doi.pangaea.de/10.1594/PANGAEA.936447, 2021.

Gallus, W. A. and Segal, M.: Impact of Improved Initialization of Mesoscale Features on Convective System Rainfall in 10-km Eta Simulations, Weather and Forecasting, 16, 680–696, https://doi.org/10.1175/1520-0434(2001)016<0680:ioiiom>2.0.co;2, 2001.

Gernhardt, S. M.: High Precision 3D Localization and Motion Analysis of Persistent Scatterers using Meter-Resolution Radar Satellite Data, Universitätsbibliothek der TU München, 2011.

Giannaros, C., Kotroni, V., Lagouvardos, K., Giannaros, T. M., and Pikridas, C.: Assessing the Impact of GNSS ZTD Data Assimilation into the WRF Modeling System during High-Impact Rainfall Events over Greece, Remote Sensing, 12, 383, https://doi.org/10.3390/rs12030383, 2020.

Giorgi, F.: Thirty Years of Regional Climate Modeling: Where Are We and Where Are We Going next?, Journal of Geophysical Research: Atmospheres, https://doi.org/10.1029/2018JD030094, 2019.

González, A., Expósito, F. J., Pérez, J. C., Díaz, J. P., and Taima, D.: Verification of precipitable water vapour in high-resolution WRF simulations over a mountainous archipelago, Quarterly Journal of the Royal Meteorological Society, 139, 2119–2133, https://doi.org/10.1002/qj.2092, 2013.

Gupta, H., Kling, H., Yilmaz, K., and Martinez, G.: Decomposition of the Mean Squared Error and NSE Performance Criteria: Implications for Improving Hydrological Modelling, Journal of Hydrology, 377, 80–91, https://doi.org/10.1016/j.jhydrol.2009.08.003, 2009.

Hanssen, R. F.: Radar interferometry - Data Interpretation and Error Analysis, vol. 2 of *Remote Sensing and Digital Image Processing*, Springer Netherlands, Dordrecht, https://doi.org/10.1007/0-306-47633-9, 2001.

Herring, T. A., King, R. W., Floyd, M. A., and McClusky, S. C.: Introduction to GAMIT/GLOBK, Release 10.7, Massachusetts Institute of Technology, Cambridge, Massachusetts, http://geoweb.mit.edu/gg/Intro_GG.pdf, 2018.

Hersbach, H., Bell, B., Berrisford, P., Hirahara, S., Horányi, A., Muñoz-Sabater, J., Nicolas, J., Peubey, C., Radu, R., Schepers, D., Simmons, A., Soci, C., Abdalla, S., Abellan, X., Balsamo, G., Bechtold, P., Biavati, G., Bidlot, J., Bonavita, M., De Chiara, G., Dahlgren, P., Dee, D., Diamantakis, M., Dragani, R., Flemming, J., Forbes, R., Fuentes, M., Geer, A., Haimberger, L., Healy, S., Hogan, R. J., Hólm, E., Janisková, M., Keeley, S., Laloyaux, P., Lopez, P., Lupu, C., Radnoti, G., de Rosnay, P., Rozum, I., Vamborg, F., Villaume, S., and Thépaut, J.-N.: The ERA5 Global Reanalysis, Quarterly Journal of the Royal Meteorological Society, n/a, https://doi.org/10.1002/qj.3803, 2020.

Heublein, M., Alshawaf, F., Erdnüß, B., Zhu, X. X., and Hinz, S.: Compressive sensing reconstruction of 3D wet refractivity based on GNSS and InSAR observations, Journal of Geodesy, 93, 197–217, https://doi.org/10.1007/s00190-018-1152-0, 2019.

Heublein, M. E. A.: GNSS and InSAR based water vapor tomography: A Compressive Sensing solution, Ph.D. thesis, Karlsruhe Institute of Technology, https://doi.org/10.5445/IR/1000093403, 2019.

Hong, S. and Lim, J. J.: The WRF single–moment 6–class microphysics scheme (WSM6), J. Korean Meteor. Soc., 42, 129–151, 2006.

Hong, S., Noh, Y., and Dudhia, J.: A new vertical diffusion package with an explicit treatment of entrainment processes, Mon. Wea. Rev., 134, 2318–2341, 2006.

Hooper, A., Segall, P., and Zebker, H.: Persistent scatterer interferometric synthetic aperture radar for crustal deformation analysis, with application to Volcán Alcedo, Galápagos, Journal of Geophysical Research, 112, B07 407, https://doi.org/10.1029/2006JB004763, 2007.

Hooper, A., Bekaert, D., Spaans, K., and Arikan, M.: Recent advances in SAR interferometry time series analysis for measuring crustal deformation, Tectonophysics, 514-517, 1–13, https://doi.org/10.1016/j.tecto.2011.10.013, 2012.

Hurter, F.: GPS based Determination of the Integrated and Spatially Distributed Water Vapor in the Troposphere, Swiss Geodetic Commission, [Geodätisch-geophysikalische Arbeiten in der Schweiz], 2004.

Hurter, F.: GNSS meteorology in spatially dense networks, Swiss Geodetic Commission, [Geodätisch-geophysikalische Arbeiten in der Schweiz], 2014.

Ide, K., Ghil, M., and Lorenc, A.: Unified Notation for Data Assimilation: Operational, Sequential and Variational, Journal of the Meteorological Society of Japan, 75, 1999.

Jade, S. and Vijayan, M.: GPS-based atmospheric precipitable water vapor estimation using meteorological parameters interpolated from NCEP global reanalysis data, Journal of Geophysical Research: Atmospheres, 113, 2008.

Jiang, X., Li, J., Li, Z., Xue, Y., Di, D., Wang, P., and Li, J.: Evaluation of Environmental Moisture from NWP Models with Measurements from Advanced Geostationary Satellite Imager—A Case Study, Remote Sensing, 12, 670, https://doi.org/10.3390/rs12040670, 2020.

Jin, S., Feng, G., and Gleason, S.: Remote sensing using GNSS signals: Current status and future directions, Advances in Space Research, 47, 1645–1653, https://doi.org/10.1016/j.asr.2011.01.036, 2011.

Jochum, A. M., Camino, E. R., de Bruin, H. A. R., and Holtslag, A. A. M.: Performance of HIRLAM in a Semiarid Heterogeneous Region: Evaluation of the Land Surface and Boundary Layer Description Using EFEDA Observations, Monthly Weather Review, 132, 2745–2760, https://doi.org/10.1175/mwr2820.1, 2004.

Jones, J., Guerova, G., Douša, J., Dick, G., de Haan, S., Pottiaux, E., and van Malderen, R.: Advanced GNSS Tropospheric Products for Monitoring Severe Weather Events and Climate, COST action ES1206 final action dissemination report, p. 563, 2019.

Klanner, L., Höveler, K., Khordakova, D., Perfahl, M., Rolf, C., Trickl, T., and Vogelmann, H.: A powerful lidar system capable of 1 h measurements of water vapour in the troposphere and the lower stratosphere as well as the temperature in the upper stratosphere and mesosphere, Atmospheric Measurement Techniques, 14, 531–555, https://doi.org/10.5194/amt-14-531-2021, 2021.

Kunz, A., Spelten, N., Konopka, P., Müller, R., Forbes, R. M., and Wernli, H.: Comparison of Fast In situ Stratospheric Hygrometer (FISH) measurements of water vapor in the upper troposphere and lower stratosphere (UTLS) with ECMWF (re)analysis data, Atmospheric Chemistry and Physics, 14, 10 803–10 822, https://doi.org/10.5194/acp-14-10803-2014, 2014.

Lindskog, M., Ridal, M., Thorsteinsson, S., and Ning, T.: Data assimilation of GNSS zenith total delays from a Nordic processing centre, Atmospheric Chemistry and Physics, 17, 13 983–13 998, https://doi.org/10.5194/acp-17-13983-2017, 2017.

Löhnert, U., Turner, D. D., and Crewell, S.: Ground-Based Temperature and Humidity Profiling Using Spectral Infrared and Microwave Observations. Part I: Simulated Retrieval Performance in Clear-Sky Conditions, Journal of Applied Meteorology and Climatology, 48, 1017–1032, https://doi.org/10.1175/2008jamc2060.1, 2009.

Massaro, G., Stiperski, I., Pospichal, B., and Rotach, M. W.: Accuracy of retrieving temperature and humidity profiles by ground-based microwave radiometry in truly complex terrain, Atmospheric Measurement Techniques, 8, 3355–3367, https://doi.org/10.5194/amt-8-3355-2015, 2015.

Mateus, P., Tomé, R., Nico, G., and Catalao, J.: Three-Dimensional Variational Assimilation of InSAR PWV Using the WRFDA Model, IEEE Transactions on Geoscience and Remote Sensing, PP, 1–8, https://doi.org/10.1109/TGRS.2016.2599219, 2016.

Mateus, P., Catalao, J., and Nico, G.: Sentinel-1 Interferometric SAR Mapping of Precipitable Water Vapor Over a Country-Spanning Area, IEEE Transactions on Geoscience and Remote Sensing, 55, 2993–2999, https://doi.org/10.1109/TGRS.2017.2658342, 2017.

Mayer, M., Knöpfler, A., Heck, B., Masson, F., Ulrich, P., and Ferhat, G.: GURN (GNSS Upper Rhine Graben Network): Research Goals and First Results of a Transnational Geo-scientific Network, in: Geodesy for Planet Earth, edited by Kenyon, S., Pacino, M. C., and Marti, U., pp. 673–681, Springer Berlin Heidelberg, Berlin, Heidelberg, https://doi.org/10.1007/978-3-642-20338-1_83, 2012.

Mlawer, E. J., Taubman, S. J., Brown, P. D., Iacono, M. J., and Clough, S. A.: Radiative transfer for inhomogeneous atmospheres: RRTM, a validated correlated–k model for the longwave, J. Geophys. Res., 102, 16 663–16 682, 1997.

Moeller, G.: Reconstruction of 3D wet refractivity fields in the lower atmosphere along bended GNSS signal paths, Phd thesis, TU Wien, Department of Geodesy and Geoinformation, http://repositum.tuwien.ac.at/obvutwoa/download/pdf/2284850, 196 p., 2017.

Ning, T., Wang, J., Elgered, G., Dick, G., Wickert, J., Bradke, M., Sommer, M., Querel, R., and Smale, D.: The uncertainty of the atmospheric integrated water vapour estimated from GNSS observations, Atmospheric Measurement Techniques, 9, 79–92, 2016.

Pacione, R. and Douša, J.: SINEX-TRO V2. 00 format description, COST Action 1206 Final Report, J, Jones et al eds, 2017.

Parker, A. L., Biggs, J., Walters, R. J., Ebmeier, S. K., Wright, T. J., Teanby, N. A., and Lu, Z.: Systematic assessment of atmospheric uncertainties for InSAR data at volcanic arcs using large-scale atmospheric models: Application to the Cascade volcanoes, United States, Remote Sensing of Environment, 170, 102–114, https://doi.org/10.1016/j.rse.2015.09.003, 2015.

Parrish, D. F. and Derber, J. C.: The National Meteorological Center's Spectral Statistical-Interpolation Analysis System, Monthly Weather Review, 120, 1747–1763, https://doi.org/10.1175/1520-0493(1992)120<1747:TNMCSS>2.0.CO;2, 1992.

Petit, G. and Luzum, B.: IERS conventions (2010), Tech. rep., Bureau International des Poids et mesures sevres (france), 2010.

Pichelli, E., Ferretti, R., Cimini, D., Panegrossi, G., Perissin, D., Pierdicca, N., Member, S., Rocca, F., and Rommen, B.: IEEE JOURNAL OF SELECTED TOPICS IN APPLIED EARTH OBSERVATIONS AND REMOTE SENSING 1 InSAR Water Vapor Data Assimilation into Mesoscale Model MM5: Technique and Pilot Study, https://doi.org/10.1109/JSTARS.2014.2357685, 2014.

Poli, P., Healy, S., Rabier, F., and Pailleux, J.: Preliminary assessment of the scalability of GPS radio occultations impact in numerical weather prediction, Geophysical Research Letters - GEOPHYS RES LETT, 35, https://doi.org/10.1029/2008GL035873, 2008.

Pondeca, M. and Zou, X.: A Case Study of the Variational Assimilation of GPS Zenith Delay Observations into a Mesoscale Model, Journal of Applied Meteorology - J APPL METEOROL, 40, 1559–1576, https://doi.org/10.1175/1520-0450(2001)040<1559:ACSOTV>2.0.CO;2, 2001.

Pospichal, B. and Crewell, S.: Boundary layer observations in West Africa using a novel microwave radiometer, Meteorologische Zeitschrift, 16, 513–523, https://doi.org/10.1127/0941-2948/2007/0228, 2007.

Prein, A. F., Langhans, W., Fosser, G., Ferrone, A., Ban, N., Goergen, K., Keller, M., Tölle, M., Gutjahr, O., Feser, F., Brisson, E., Kollet, S., Schmidli, J., Lipzig, N. P. M., and Leung, R.: A review on regional convection-permitting climate modeling: Demonstrations, prospects, and challenges, Rev. Geophys., 53, 323–361, https://doi.org/10.1002/2014RG000475, 2015.

Qin, Y., Perissin, D., and Lei, L.: InSAR X-band atmospheric Water Vapor analysis and comparison in Hong Kong, in: International Geoscience and Remote Sensing Symposium (IGARSS), pp. 125–128, https://doi.org/10.1109/IGARSS.2013.6721108, 2013.

Randel, D. L., Greenwald, T. J., Haar, T. H. V., Stephens, G. L., Ringerud, M. A., and Combs, C. L.: A New Global Water Vapor Dataset, Bulletin of the American Meteorological Society, 77, 1233–1246, https://doi.org/10.1175/1520-0477(1996)077<1233:angwvd>2.0.co;2, 1996.

Reale, A., Tilley, F., Ferguson, M., and Allegrino, A.: NOAA operational sounding products for advanced TOVS, International Journal of Remote Sensing, 29, 4615–4651, https://doi.org/10.1080/01431160802020502, 2008.

Rocken, C., Kuo, Y.-H., Sokolovskiy, S. V., and Anthes, R. A.: The ROCSAT-3/COSMIC mission and applications of GPS radio occultation data to weather and climate, in: Remote Sensing Applications of the Global Positioning System, edited by Bevis, M., Shoji, Y., and Businger, S., SPIE, https://doi.org/10.1117/12.566544, 2004.

Saastamoinen, J.: Atmospheric correction for the troposphere and stratosphere in radio ranging satellites, The use of artificial satellites for geodesy, 15, 247–251, 1972.

Schaer, S.: Mapping and predicting the Earth's ionosphere using the Global Positioning System, vol. 59, Institut für Geodäsie und Photogrammetrie, Eidg. Technische Hochschule . . . , 1999.

Schmid, R., Dach, R., Collilieux, X., Jäggi, A., Schmitz, M., and Dilssner, F.: Absolute IGS antenna phase center model igs08. atx: status and potential improvements, Journal of Geodesy, 90, 343–364, 2016.

Shehaj, E., Wilgan, K., Frey, O., and Geiger, A.: A collocation framework to retrieve tropospheric delays from a combination of GNSS and InSAR, NAVIGATION, 67, 823– 842, https://doi.org/https://doi.org/10.1002/navi.398, 2020.

Shi, L., Matthews, J., peng Ho, S., Yang, Q., and Bates, J.: Algorithm Development of Temperature and Humidity Profile Retrievals for Long-Term HIRS Observations, Remote Sensing, 8, 280, https://doi.org/10.3390/rs8040280, 2016.

Simmons, A. and Gibson, J.: The era-40 project plan. ERA-40 project report series 1, ECMWF, Reading, United Kingdom, 63, 2000.

Skamarock, W. C. and Klemp, J. B.: A time-split nonhydrostatic atmospheric model for weather research and forecasting applications, Journal of Computational Physics, 227, 3465–3485, https://doi.org/10.1016/j.jcp.2007.01.037, 2008.

SNAP: S1TBX - ESA Sentinel-1 Toolbox v8.0.1, http://step.esa.int/, [Online; accessed 01 February 2021], 2021.

Steinke, S., Eikenberg, S., Löhnert, U., Dick, G., Klocke, D., Girolamo, P. D., and Crewell, S.: Assessment of small-scale integrated water vapour variability during HOPE, Atmospheric Chemistry and Physics, 15, 2675–2692, https://doi.org/10.5194/acp-15-2675-2015, 2015.

Steinke, S., Wahl, S., and Crewell, S.: Benefit of high resolution COSMO reanalysis: The diurnal cycle of column-integrated water vapor over Germany, Meteorologische Zeitschrift, 28, 165–177, https://doi.org/10.1127/metz/2019/0936, 2019.

Stevens, B. and Bony, S.: Water in the atmosphere, Physics Today, 66, 29–34, https://doi.org/10.1063/PT.3.2009, 2013.

Teunissen, P. and Montenbruck, O.: Springer Handbook of Global Navigation Satellite Systems, Springer, 2017.

Thébault, E., Finlay, C. C., Beggan, C. D., Alken, P., Aubert, J., Barrois, O., Bertrand, F., Bondar, T., Boness, A., Brocco, L., et al.: International geomagnetic reference field: the 12th generation, Earth, Planets and Space, 67, 1–19, 2015.

Vogelmann, H., Sussmann, R., Trickl, T., and Reichert, A.: Spatiotemporal variability of water vapor investigated using lidar and FTIR vertical soundings above the Zugspitze, Atmospheric Chemistry and Physics, 15, 3135–3148, https://doi.org/10.5194/acp-15-3135-2015, 2015.

Wagner, A., Heinzeller, D., Wagner, S., Rummler, T., and Kunstmann, H.: Explicit Convection and Scale-Aware Cumulus Parameterizations: High-Resolution Simulations over Areas of Different Topography in Germany, Monthly Weather Review, 146, 1925–1944, https://doi.org/10.1175/MWR-D-17-0238.1, 2018.

Wagner, A., Fersch, B., Yuan, P., Rummler, T., and Kunstmann, H.: Assimilation of GNSS and Synoptic Data in a Convection Permitting Limited Area Model: Improvement of Simulated Tropospheric Water Vapor Content, Frontiers in Earth Science, 10, https://doi.org/10.3389/feart.2022.869504, 2022.

Wang, J., Zhang, L., and Dai, A.: Global estimates of water-vapor-weighted mean temperature of the atmosphere for GPS applications, Journal of Geophysical Research: Atmospheres, 110, 2005.

Yuan, P., Hunegnaw, A., Alshawaf, F., Awange, J., Klos, A., Teferle, F. N., and Kutterer, H.: Feasibility of ERA5 integrated water vapor trends for climate change analysis in continental Europe: An evaluation with GPS (1994–2019) by considering statistical significance, Remote Sensing of Environment, 260, 112 416, 2021.

Zhou, L., Lin, S.-J., Chen, J.-H., Harris, L. M., Chen, X., and Rees, S. L.: Toward Convective-Scale Prediction within the Next Generation Global Prediction System, Bulletin of the American Meteorological Society, 100, 1225–1243, https://doi.org/10.1175/bams-d-17-0246.1, 2019.

Zhu, M., Liu, Z., and Hu, W.: Observing Water Vapor Variability During Three Super Typhoon Events in Hong Kong Based on GPS Water Vapor Tomographic Modeling Technique, Journal of Geophysical Research: Atmospheres, 125, e2019JD032 318, 2020.